Contents lists available at ScienceDirect

Applied Catalysis B: Environmental

Enhanced photocatalytic mechanism of the Nd-Er co-doped tetragonal $BiVO_4$ photocatalysts

Ting Liu[a], Guoqiang Tan[a,*], Chengcheng Zhao[a], Chi Xu[a], Yuning Su[a], Ying Wang[a], Huijun Ren[b], Ao Xia[a], Dan Shao[a], Shemin Yan[c]

[a] School of Materials Science and Engineering, Shaanxi University of Science & Technology, Xi'an 710021, China
[b] School of Arts and Sciences, Shaanxi University of Science & Techology, Xi'an 710021, China
[c] Xianyang Research & Design Institute of Ceramics, Xian yang 712000, China

ARTICLE INFO

ABSTRACT

The Nd/Er co-doped tetragonal $BiVO_4$ photocatalysts are synthesized by a microwave hydrothermal method, and the crystal structures, morphologies and optical properties are characterized. The substitution of Nd^{3+} and Er^{3+} for Bi^{3+} sites leads to distortion of the $[VO_4]$ tetrahedron chains and induces the monoclinic structure transforming into the tetragonal structure, with the morphology evolving from nano particle agglomerations to disorganized regular rods agglomerations. The impurity energy levels induced by Nd^{3+} and Er^{3+} in the energy band of $BiVO_4$ act as electron traps and have further energy transfer in the up-conversion processes to facilitate the photocarriers' separation. The more positive VB positions in the co-doped $BiVO_4$ band structures can also effectively enhance oxidation capacity. Based on the above synergetic effect, the degradation rate the degradation rate of co-doped tetragonal $BiVO_4$ photocatalyst can reach the highest 96% within 150 min under simulated sunlight and 20 min under the NIR irradiation.

1. Introduction

In recent years, the increasing energy and environmental problems have threatened the development of ecological civilization. Especially the water pollution has become an urgent crisis to overwhelm in the world. However, the traditional semiconductor TiO_2 has a too narrow optical response range to expand its application in water pollutant abatement [1,2]. Fortunately, bismuth vanadate ($BiVO_4$) has been considered by researchers as an attractive visible light responsive photocatalyst [3]. According to the previous literatures [4,5], it is known that $BiVO_4$ has three crystalline phases, including monoclinic scheelite, tetragonal zircon and tetragonal scheelite. Generally, the monoclinic $BiVO_4$ (m-$BiVO_4$) with the band gap of 2.4 eV caused by the valence band of Bi 6s and O 2p possesses the excellent catalytic potential over the other two phases [6,7]. However, the undesirable recombination of electrons and holes, and the low quantum efficiency are still two main drawbacks of m-$BiVO_4$. While under special cases, t-$BiVO_4$ can show higher photocatalytic properties, such as rare earth doped $BiVO_4$.

Recently, researchers have made some progress in rare earth doped $BiVO_4$ photocatalysts, such as La [8], Tb [9], Gd [10], Tm [11], Dy [12], Y [13,14], Eu [15], Er [14] and Ce [16] et al., due to the rich energy levels and special 4f electronic transition properties. Sara et al. reported that the $BiVO_4$ with higher catalytic activity was obtained due to the Y^{3+} doped into both m/t-$BiVO_4$ [17]. It demonstrated that the Y^{3+} doped heterostructured $BiVO_4$ exhibited the lower charge carrier recombination. According to our previous study, most rare earth elements can transform m-$BiVO_4$ into much more active t-$BiVO_4$ [10,18]. Especially, both Nd-$BiVO_4$ and Er-$BiVO_4$ catalysts can induce up-conversion characters and enhance carrier concentrations, thus improve the photocatalytic property [19,20]. The up-conversion materials can absorb lower energy light (such as NIR or visible range) and emit the higher energy light (such as visible or UV range), improving the photons absorption. Based on the contribution of extra-photons generated by the luminescence process, the conjunction mechanism of electronic and luminescence of Er-$BiVO_4$ was proposed to enhance photocatalystic efficiencies by Sergio et al. [21]. Therefore, the up-conversion effect can be evaluated by luminescence characteristics.

In addition to single-doped rare earth, co-doping with different types of ions has also been reported by many researchers to investigate the synergetic effects between co-doped ions. Shan et al. proposed that core–shell structured $BiVO_4$ induced by Er^{3+}/Yb^{3+}

dopants exhibited the enhanced charge carrier mobility [22]. The dopants of Er^{3+} and Yb^{3+} in the shell can suppress the recombination process and lead to the higher photon efficiency. S. Obregón et al. reported a highly active monoclinic-tetragonal $BiVO_4$ heterostructur system by doping Yb^{3+} and Er^{3+}, and the enhancement of photocatalytic performance is mainly attributed to a double mechanism of monoclinic/tetragonal $BiVO_4$ heterojunction structure and supportive photoluminescence up-conversion process [23]. However, rare literatures have reported the co-doping of Nd^{3+} and Er^{3+} to modify $BiVO_4$, and the further correlation between Nd^{3+} and Er^{3+} needs to be explored.

In this paper, we studied the Nd/Er $BiVO_4$ photocatalyst through a microware hydrothermal and assessed the photoactivity in the environment. The formed impurity levels of Nd^{3+} and Er^{3+} in $BiVO_4$ are mainly studied, especially the effects of Nd^{3+} and Er^{3+} in $BiVO_4$ on light absorption and energy structure properties has been investigated via the optical and photoelectrochemical measurements.

2. Experimental section

2.1. Preparations

Nd/Er co-doped $BiVO_4$ system photocatalysts with various molar ratios of Nd and Er elements were prepared by a microwave hydrothermal method, and the detailed steps are as follows. Firstly, 0.01 mol of $Bi(NO_3)_3 \cdot 5H_2O$ and NH_4VO_3 were dissolved into deionized water with magnetic stirring for 30 min, respectively and then mixed them. Secondly, NaOH solution (1 M) was added into the above suspension to adjust the pH value to 7 with vigorous stirring for 60 min. Then, x mmol of $Nd(NO_3)_3 \cdot 6H_2O$ and y mmol of $Er(NO_3)_3 \cdot 6H_2O$ were dissolved into the above solution with stirring for 60 min to get the homogeneous solution (x = 1, 0.4, 0.5, 0.6, 0, y = 0, 0.6, 0.5, 0.4, 1). Subsequently, the solution was transferred into the Teflon vessel and heated at 180 °C for 40 min, and then naturally cooled until room temperature. The precipitates were filtered and washed repeatedly. Finally, the samples were dried at 80 °C for 6 h. The samples with x = 0, 1, 0.4, 0.5, 0.6, 0 were $BiVO_4$, 10%Nd-$BiVO_4$, 4%Nd + 6%Er-$BiVO_4$, 5%Nd + 5%Er-$BiVO_4$, 6%Nd + 4%Er-$BiVO_4$ and 10%Er-$BiVO_4$, which would be denoted as BVO, 10%Nd-BVO, 4%Nd + 6%Er-BVO, 5%Nd + 5%Er-BVO, 6%Nd + 4%Er-BVO and 10%Er-BVO, respectively. And the 10%Nd-BVO and 10%Er-BVO were denoted as doped BVO, while the 4%Nd + 6%Er-BVO, 5%Nd + 5%Er-BVO and 6%Nd + 4%Er-BVO were denoted as co-doped BVO.

2.2. Characterization

The crystalline structures of the samples were monitored by an X-ray diffraction (XRD, D/max-2200PC, Rigaku, Cu Kα, λ = 0.15406 nm, 40 kV, 40 mA) in the range of 15–70°. The morphologies characterizations were measured by a field emission scanning electron microscopy (FE-SEM, S4800, Japan). The microstructures analyses were performed on a transmission electron microscopy (TEM, FEI TECNAI G2F20 S-TWIN, U.S.A.). The Raman scattering spectra (Renishaw invia) measurements were detected by excitations with 532 nm and 785 nm. The element contents analyses were carried out with an inductively coupled plasma atomic emission spectroscopy (ICP-AES, Agilent 5100, Australia). The surface analysis was measured by X-ray photoelectron spectroscopy (XPS) (Model XSAM800, Shimadzu-Kratos Ltd., Japan). The UV–vis Diffuse Reflectance Spectra (DRS, Cray 5000, Agilent, U.S.A.) were recorded in the wavelength range of 200–800 nm to study the optical absorption range. The photoluminescence (PL, F-4600, Japan) spectra of photocatalysts were determined on a fluorescence spectrophotometer at an excitation wavelength of 375 nm.

The photocatalytic activities of catalysts were evaluated by the degradation of Rhodamine (RhB) in aqueous solution under the simulated sunlight irradiation using a 500 W xenon lamp (190 nm < λ < 1100 nm), which was conducted in an XPA-7 photochemical reactor. Another photodegradation was studied using higher intensity LED lamp at narrow wavelength (green light, λ = 535 nm). In this experiment, 50 mg of the catalyst was added into 50 mL aqueous of RhB (10 mg L^{-1}) in a quartz tube and stirred in darkness for 30 min before illumination to establishment of adsorption-desorption equilibrium between photocatalysts and RhB molecules. During the photoreaction, the RhB solution with photocatalysts was continuously stirred with a dynamoelectric stirrer, and 10 mL of the suspension was collected at a certain time, followed by centrifugation (3500 r·min^{-1}) for 15 min and filtration to remove the photocatalyst particles. The concentration was analyzed by measuring the maximal absorbance at 554 nm for RhB using a SP-756P spectrophotometer.

2.3. Electrochemical analyses

Mott-Schottky measurement was conducted on an electrochemical workstation (CHI-660E, China) with a standard three-electrode cell. A platinum foil and an Ag/AgCl electrode were used as the counter electrode and reference electrode respectively. The BVO, 10%Nd-BVO, 10%Er-BVO and 5%Nd + 5%Er-BVO were dissolved into a uniform suspension solution to coat on a 1.5 × 2 cm^2 FTO/glass substrate. The preparation method of electrodes would be presented in detail as follows. 0.1 g of aforesaid samples was dissolved into the mixed solution of 1 mL of anhydrous ethanol and 0.1 mL of acetyl acetone, and a uniform suspension was obtained with the ultrasonic dispersion. Then the as-prepared suspension was coated on a FTO conducting glass. The film electrodes were dried under ambient air condition and then calcinated at 200 °C for 3 h. The 0.1 M Na_2SO_4 aqueous solution was used as an electrolyte. An Xe lamp (300 W) was used as the simulated sunlight source and it with the filer as the NIR source (750–1500 nm).

3. Results and discussion

Fig. 1 presents the XRD patterns of $BiVO_4$ samples. It can be seen that the BVO has a monoclinic structure (JDPDS No.75-1866), while the tetragonal structure (JDPDS No.14-0133) can be detected in doped BVO and co-doped BVO. The results of XRD patterns suggest that Nd or Er ions co-doping can induce a phase transition from a monoclinic- to a tetragonal-$BiVO_4$. The tetragonal $NdVO_4$ and $ErVO_4$ seeds with the higher reaction diving force definitely dominate the formation of tetragonal Nd/Er-$BiVO_4$ [19,20]. And the co-doped BVO samples have broader diffraction peaks compared with the doped BVO. Subsequently, the crystallite sizes of all samples can be estimated using the Scherrer formula [24] (1):

$$D_{hkl} = \frac{K\lambda}{\beta \cos \theta} \tag{1}$$

As a consequence, the crystallite size of tetragonal $BiVO_4$ is estimated to be 54.1 nm, and that of 10%Nd-BVO, 10%Er-BVO, 4%Nd + 6%Er-BVO, 5%Nd + 5%Er-BVO and 6%Nd + 4%Er-BVO samples are 44.8, 36.9, 35.1, 34.9 and 30.3 nm, respectively. The crystallite sizes of co-doped BVO present a tendency of diminution to different degrees. It can be concluded that the kinetic energy requirement for dual-irons doping into lattice $BiVO_4$ in co-doped BVO samples is higher than that of doped BVO, which reduces the co-doped BVO crystal growth energy. This lattice distortion also indicates that there are defects in the $BiVO_4$ grains. In addition, no diffraction peaks of Nd or Er-contained compounds are detected, probably due to its trace amount or just presenting as Nd^{3+} or Er^{3+}. Fig. 1b portrays the magnified XRD patterns at 2θ = 24.4° corresponding to
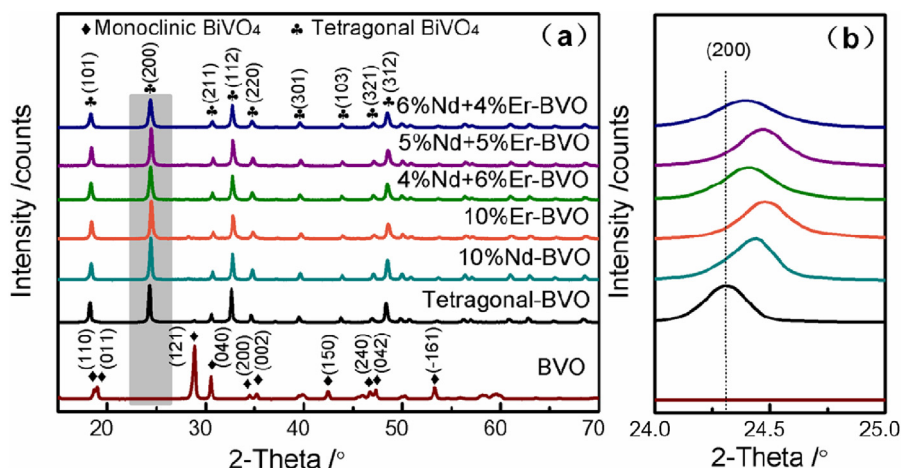
Fig. 1. X-ray diffraction patterns of $BiVO_4$ samples.

(200) diffraction peaks of the doped/co-doped BVO. The diffraction peaks of doped and co-doped BVO are slight right shifted than BVO, while the boarder diffraction peaks of the co-doped BVO are higher than those of the doped BVO. This may be due to the internal stress left by the crystallization of $NdVO_4$ and $ErVO_4$ during the phase transformation so that the Nd^{3+}/Er^{3+} co-doping leads to a structure aberration in the $BiVO_4$ crystal structure [25].

The cell parameters of $BiVO_4$ samples can be calculated with Rietveld refinement using XRD data, as listed in Table 1. In the light of the refinement results, c parameter of the doped/co-doped tetragonal BVO shows a notable diminution that the cell volume is more strongly decreased than that of the BVO (shown in Table 1). The phenomenon has already been stated that the rare element doping could change cell parameters of the crystal [26]. As the ionic radius of Bi^{3+} (0.110 nm) is slightly larger than that of Nd^{3+} (0.099 nm) and Er^{3+} (0.103 nm) [21,27–29], the tetragonal $BiVO_4$ has the lattice distortion and the diminished crystallite size because of the replacement of Bi^{3+} sites by Nd^{3+} and Er^{3+}. The decrease of the crystal cell size is attributed to the existence of Bi-O-RE bonds at the interfaces, which prevents $BiVO_4$ from adhering together and inhibits the growth of crystal grains. Consequently, the substitution of Nd^{3+} and Er^{3+} for the Bi^{3+} sites leads to the $[VO_4]$ tetrahedron chains distortion and induces the transformation from monoclinic-into tetragonal- structure [16].

In order to characterize the morphology characteristics, FE-SEM, TEM, HRTEM and SAED images of all the samples are shown in Fig. 2. From the view of FESEM images, the BVO sample is composed of irregular nanosheets with the surface size of about 200–1000 nm (Fig. 2a). The TEM image of BVO (Fig. 2b) shows that the nanosheets are decorated by thinner irregular sheets and stacked up with each other. And the clear and well-defined diffraction spots indicate that the BVO is a single crystal structure (the inset of Fig. 2b). From the TRTEM image, the clear lattice spacing of 0.261 nm can be observed on the nanosheets which corresponds to the (002) planes of monoclinic $BiVO_4$ (Fig. 2c). The morphologies of the doped BVO clearly denote that the sheet-like structure has been destroyed into nano-small particles agglomerations with a small part of rod-like structure (Fig. 2d, e). The co-doped BVO appear more regular and dispersive rods with the larger length to diameter ratios and smaller cross sections (Figs. 2 f, S1a–b). However, the different degrees of rod-like agglomeration are observed in the 4%Nd + 6%Er-BVO and 6%Nd + 4%Er-BVO samples. Especially, 5%Nd + 5%Er-BVO has the most regular rods structure with less residue nano particles compared with the other co-doped BVO samples. The further TEM and HRTEM analyses of 5%Nd + 5%Er-BVO show that there is no great change (Fig. 2g). Another lattice spacing of 0.368 nm can be assigned

to tetragonal $BiVO_4$ (200) crystal plane (Fig. 2h) [30]. Combined with above structure analyses, induced by Nd^{3+} and Er^{3+} replacement for Bi^{3+} sites, the distortion of $[VO_4]$ tetrahedrons leads to the external morphologies evolution from particle aggregates into rod-particle aggregates. The corresponding elemental analysis (Fig. 2i) indicates that existence of Bi, V and O in BVO, 10%Nd-BVO, 10%Er-BVO and 5%Nd + 5%Er-BVO samples. In addition, doped BVO possess the element of Nd or Er and 5%Nd + 5%Er-BVO is composed of Nd and Er.

The Raman spectroscopy is used to probe the vibrational properties of BVO, 10%Nd-BVO, 10%Er-BVO and 5%Nd + 5%Er-BVO, as shown in Fig. 3. The five signals are Raman bands characteristics of monoclinic $BiVO_4$ (Fig. 3a). It can be observed that the BVO bands at 132 and 216 cm^{-1} are assignable to the rotation/translation modes of $BiVO_4$. And the bands at 329, 372 and 830 cm^{-1} can be assigned to the asymmetric and symmetric deformation modes of the VO_4^{3-} tetrahedron and stretching vibrations of V-O bonds, respectively [31,32]. The bands at 855 nm of 10%Nd-BVO is assigned to V-O symmetric stretching mode of tetragonal $BiVO_4$ [33]. At 350–750 nm^{-1}, the shapes of 10%Er-BVO and 5%Nd + 5%Er-BVO are quite different from that of BVO (inset of Fig. 3a), with no typical peaks of tetragonal $BiVO_4$ but appearing the fluorescence peaks of Er^{3+} [34]. Furthermore, the 10%Nd-BVO, 10%Er-BVO and 5%Nd + 5%Er-BVO are excited by 785 nm red laser (Fig. 3b). Only 10%Er-BVO can markedly show the typical tetragonal $BiVO_4$ bands at 256, 374 and 864 cm^{-1}. Similarly, 10%Nd-BVO and 5%Nd + 5%Er-BVO reveal the luminescence peaks in the range of 300–800 nm induced of Nd^{3+} (insert of Fig. 3b). Such a luminescence phenomenon can indicate that Fig. 3 is not only a Raman spectrum, but also the reflection of emission due to electron transition at Nd^{3+} and Er^{3+} levels [35]. Likewise, it can be pointed out again that Nd and Er are present as ionic states in tetragonal $BiVO_4$.

X-ray photoelectron spectroscopy (XPS) is determined the chemical states of BVO and doped/co-doped BVO samples (Fig. 4a–f). As for the survey spectra (Fig. 4a), the elements of Bi, V, O, Nd and Er are detected on the surface of the samples. The obtained binding energies analyses in XPS are rectified by reference to a C 1s value of 284.6 eV. From the high-resolution XPS spectra of Bi (Fig. 4b), two symmetric peaks at 158.9 eV and 164.2 eV are attributed to the Bi $4f_{7/2}$ and Bi $4f_{5/2}$, respectively [36], indicating the presence of Bi^{3+} in $BiVO_4$. The two peaks in the V 2p spectra (Fig. 4c) shows a binding energy at 516.1 eV assigned to the V$2p_{3/2}$, proving V element is present as V^{5+}. In the O 1s XPS spectra (Fig. 4d), the region of 528–536 eV could be fitted into two signals at 531.2 eV, and 533 eV assign to lattice oxygen (O_{latt}) and adsorbed oxygen (O_{ads}), respectively. Compared to the BVO, two

Table 1
Structural parameters, energy gaps and degradation rates of BiVO$_4$ samples.

| samples	Space group	Crystal struture	Cell parameters			Rw (%)	Cell volume (Å^3)	Band gap (eV)
			a	b	c			
BVO	I2/b	Monoclinic	5.1956	5.0976	11.6901	10.37	309.62	2.4
10%Nd-BVO	I41/a	Tetragonal	7.3122	7.3122	6.4610	11.87	345.45	2.8
10%Er-BVO	I41/a	Tetragonal	7.3005	7.3005	6.4583	14.66	344.21	2.8
4%Nd + 6%Er-BVO	I41/a	Tetragonal	7.2961	7.2961	6.4512	14.27	343.42	2.8
5%Nd + 5%Er-BVO	I41/a	Tetragonal	7.3041	7.3041	6.4575	12.36	344.51	2.8
6%Nd + 4%Er-BVO	I41/a	Tetragonal	7.3067	7.3067	6.4615	13.82	344.97	2.8
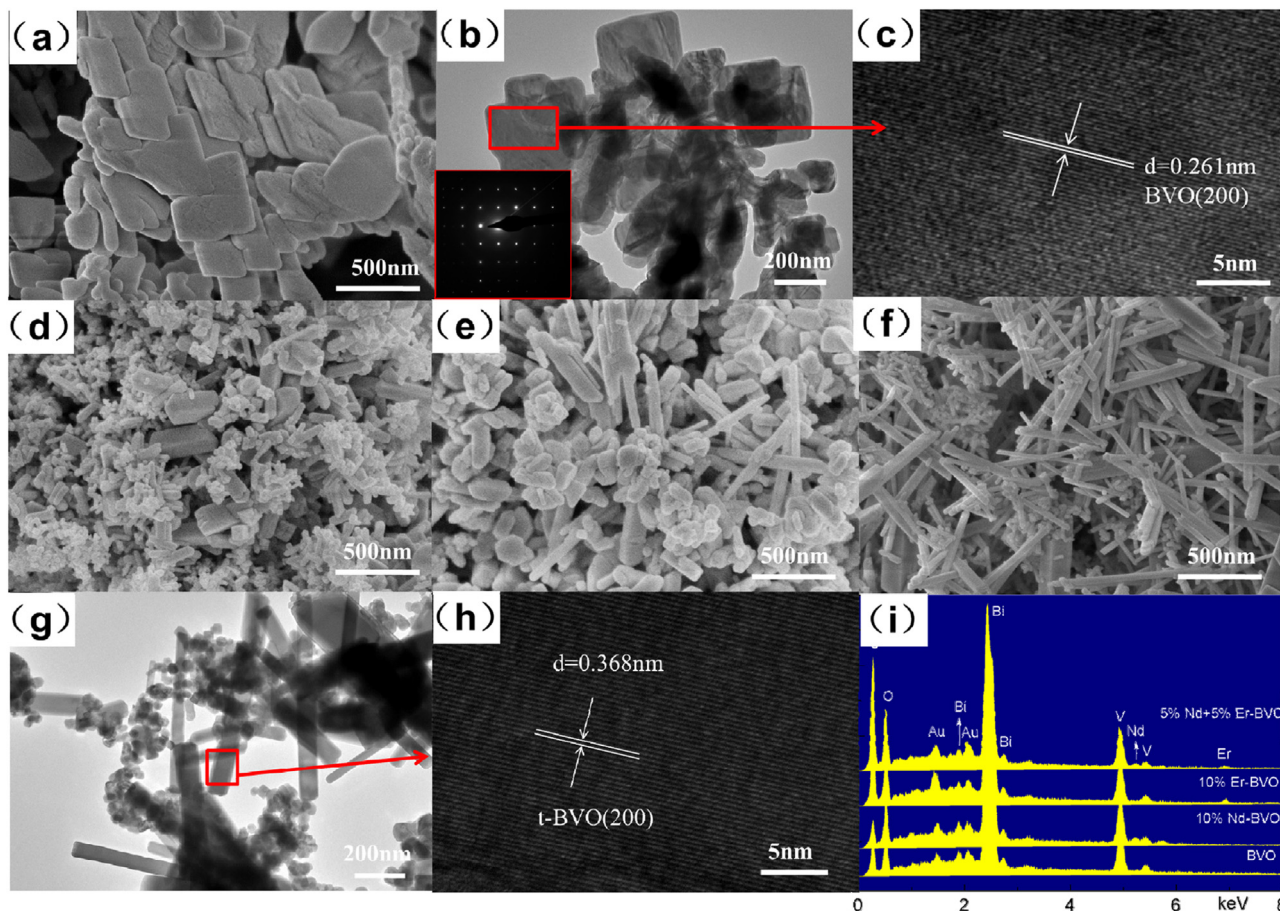
Fig. 2. SEM, TEM, HRTEM, SAED images for BiVO$_4$ samples BVO (a–c), 10%Nd-BVO (d), 10%Er-BVO (e), 5%Nd + 5%Er-BVO (f–h) and EDS spectra (i) for BVO, 10%Nd-BVO, 10%Er-BVO and 5%Nd + 5%Er-BVO.
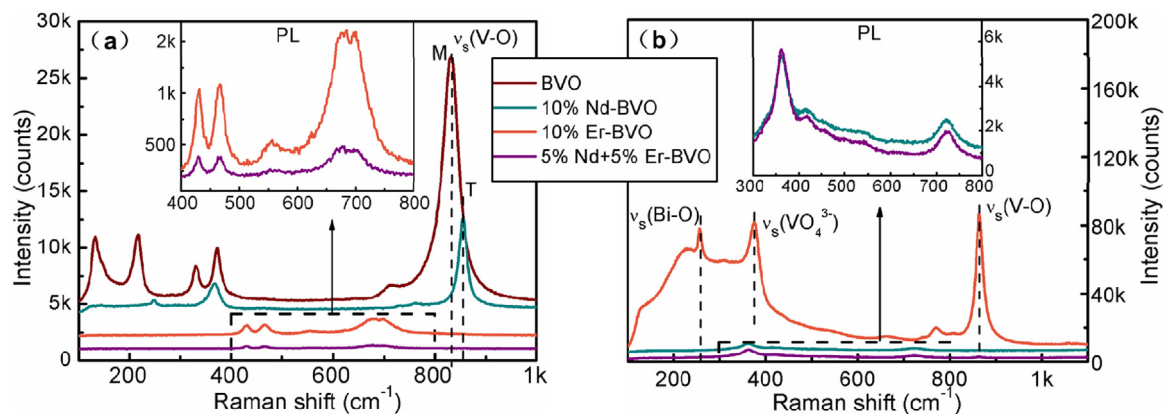

Fig. 3. Raman spectra for BVO, 10%Nd-BVO, 10%Er-BVO and 5%Nd + 5%Er-BVO under (a) green laser (532 nm) excitation; (b) red laser (785 nm) excitation.
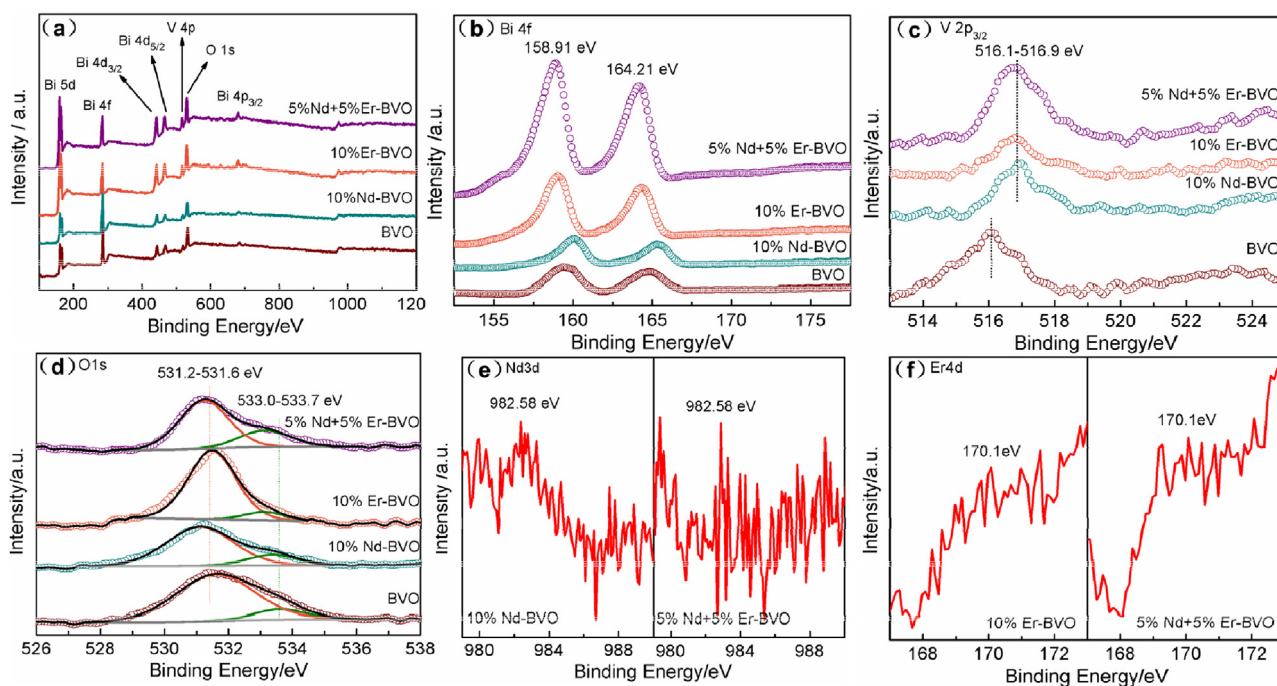
Fig. 4. XPS spectra of BVO, 10%Nd-BVO, 10%Er-BVO and 5%Nd + 5%Er-BVO samples for (a) survey spectrum, (b) Bi 4f, (c) V2p3/2, (d) O 1s, (e) Nd 3d, and (f) Er 4d.

peaks observed at 982.6 and 170.1 eV are attributed to the Nd^{3+} and Er^{3+} in 10%Nd-BVO, 10%Er-BVO and 5%Nd + 5%Er-BVO (Fig. 4e-f), respectively. However, there is indeed a problem where Er^{3+}'s peak is not obvious.

Thus, the concrete contents of Nd, Er, Bi and V for 10%Nd-BVO, 10%Er-BVO and 5%Nd + 5%Er-BVO samples are further established with inductively coupled plasma atomic emission spectroscopy (ICP-AES). The mass percentage of Bi, V, Nd and Er elements for samples are shown in Table 2 according to the theoretical calculation of them. In addition, since Er and Nd induce lattice distortion, and the consistency of theoretical and practical content, it also can deduce that the valence state of Er is also +3.

Photocatalytic activities of the $BiVO_4$ samples are measured by detecting the optical absorption changes at 554 nm of the RhB solution during its degradation process under the simulated sunlight, as shown in Fig. 5a. Accordingly, it has been calculated that the degradation efficiencies of the BVO, 10%Nd-BVO, 10%Er-BVO, 4%Nd + 6%Er-BVO, 5%Nd + 5%Er-BVO, 6%Nd + 4%Er-BVO are 57.51%, 40.78%, 63.45%, 84.50%, 96.19% and 85.80%, respectively. 10%Er-BVO displays the relatively poor degradation efficiency induced by the simulated sunlight, even lower than that of BVO. By contrast, the co-doped BVO samples do show the better photocatalytic behaviors. Especially the 5%Nd + 5%Er-BVO sample shows the highest photocatalytic degradation rate, which is over 96% within 150 min irradiation. In addition, the absorbance curve of 5%Nd + 5%Er-BVO appears to be obvious blue shift (in the inset of Fig. 5a), which can be attributed to the consecutive de-ethylation process of RhB molecules during the degradation [37].

Then, to confirm the stability of the high photocatalytic performance of the 5%Nd + 5%Er-BVO, the circulating runs in the photocatalytic degradation of RhB under simulated the sunlight are carried out and shown in Fig. 5b. After three recycles of the photodegradation of RhB, the activity of this sample only exhibits a slight decrease. It indicates that the 5%Nd + 5%Er-BVO has good photostability, which is especially important for its application.

To further investigate the relationship among the roles of these active species in degradation process, ethylene diaminetetraacetic acid (EDTA), benzoquinone (BQ) and Tert-butyl alcohol (TBA), as the

scavengers of h^+, $O^{2-}\bullet$ and $\bullet OH$ respectively, are added to the system to understand the photocatalytic mechanism (Fig. 5c). When the TBA is added, the degradation rate of RhB has no obvious change, has only slightly decreased with the added BQ but decreased greatly in the sample with EDTA. From the above results, it can be found that h^+ is the main active species in the degradation followed by the $O^{2-}\bullet$, while $\bullet OH$ contributes a little to the photocatalytic process in the 5%Nd + 5%Er-BVO. The RhB molecules are degraded by h^+ and $O^{2-}\bullet$ into small molecules.

In order to further explore the relationship between photocatalytic degradation rates and the surface area of $BiVO_4$ samples, kinetics constants of the degradation process and BET surface areas are measured (Fig. 5d). It is obvious that the specific surface area of the doped BVO increases, but the kinetic constants are not increased correspondingly. With the largest surface areas of 10%Nd-BVO, its photodegradation rate is less than those of co-doped BVO samples. It is also worthy of noting that the 5%Nd + 5%Er-BVO possesses the highest kinetic constant but its surface area is lower than those of doped/co-doped BVO except for 10%Er-BVO. The tendency between specific surface area and the crystallite size from XRD analyses is not well corresponded due to the presence of agglomeration of the $BiVO_4$ particles. All this deduces that the two factors of surface area and morphology are not found to be important factors for the photocatalytic degradation process.

Fig. 6a shows the UV–vis diffuse reflectance spectra (DRS) of the all $BiVO_4$ samples. BVO exhibits a steep absorption edge located at the wavelength of 510 nm, while doped/co-doped BVO samples located at almost the same wavelength of 432 nm possess stronger absorptions in the UV region. Fig. 6b exhibits the magnified absorption spectra of doped/co-doped BVO samples at the range of 450–800 nm. In the doped/co-doped BVO samples, four peaks at 530 nm, 593 nm, 687 nm and 754 nm are assigned to the transition from the $^4I_{9/2}$ ground state of Nd^{3+} to the high energy levels $^4G_{7/2}$, $^4G_{5/2}$, $^4F_{9/2}$ and $^4F_{7/2}$ excited states. The three peaks at 488 nm, 523 nm and 659 nm are attributed to Er^{3+} state transition from the $^4I_{15/2}$ ground state to the high energy levels $^4F_{7/2}$, $^2H_{11/2}$ and $^4F_{9/2}$ excited states, respectively. According to the reported phenomena of doping La^{3+} induced up-conversion property [19,20], it can be

Table 2
ICP-AES results of 10%Nd-BVO, 10%Er-BVO and 5%Nd + 5%Er-BVO samples.

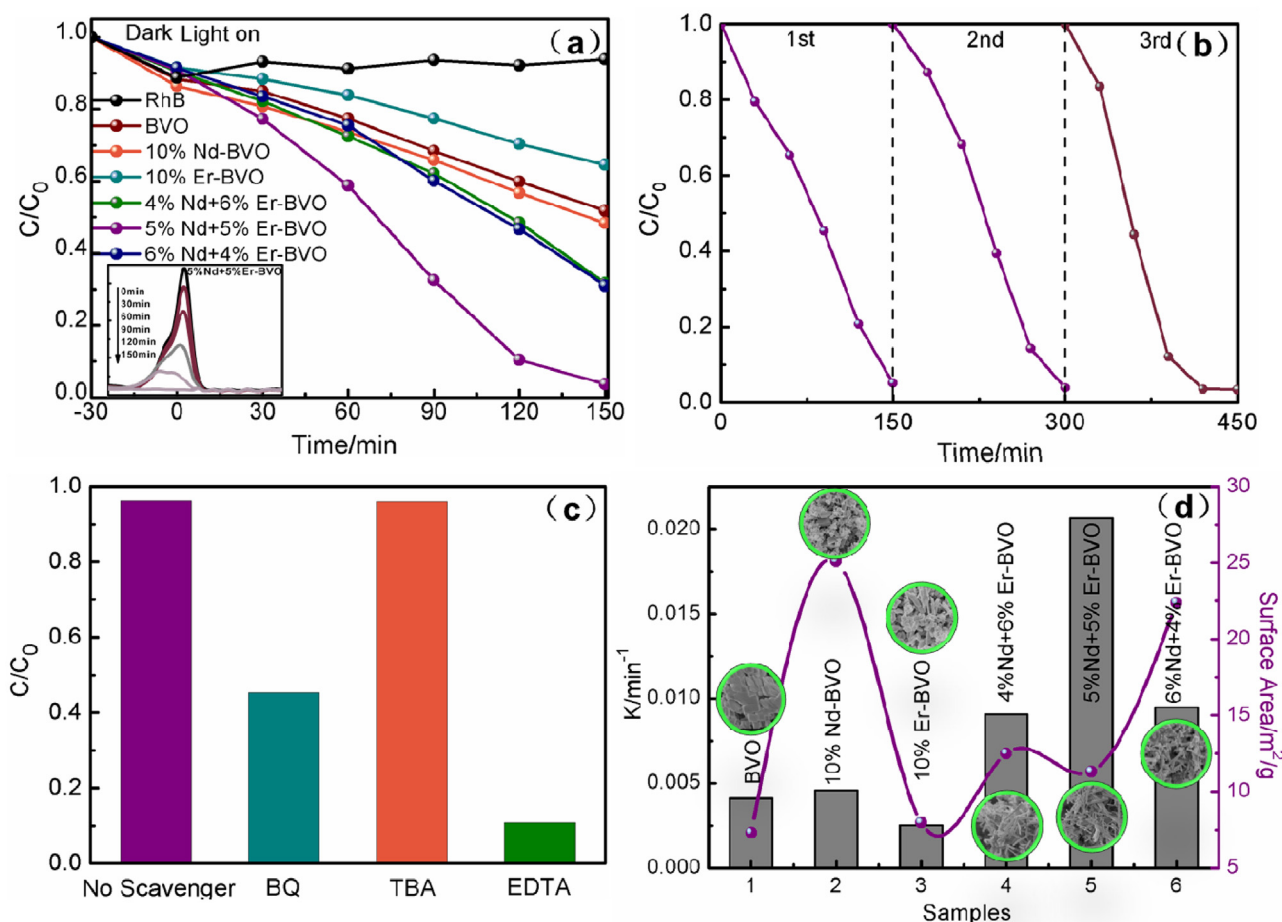| Samples	Contents							
	Test data (wt%)					Theoretical data (wt%)		
	Bi	V	Nd	Er	Bi	V	Nd	Er
10%Nd-BVO	57.46	15.09	4.39	–	59.25	16.05	4.54	–
10%Er-BVO	40.55	14.80	–	4.85	58.82	15.93	–	5.23
5%Nd + 5%Er-BVO	64.61	14.12	2.11	2.65	59.04	15.99	2.26	2.63

Fig. 5. (a) Photodegardation curves of RhB using $BiVO_4$ samples (b) Recycling test for the photodegradation of RhB on 5%Nd + 5%Er-BVO (c) Photocatalytic degradation of RhB over 5%Nd + 5%Er-BVO with the addition of BQ, TBA, and EDTA (d) The kinetics constants of photodegradation and surface areas of $BiVO_4$ samples under the simulated sunlight.

deduced that the up-conversion characteristic exists in doped/co-doped BVO samples. The band gap values of $BiVO_4$ samples (Table 1) are calculated by the formula $Eg = 1240.8/\lambda$ (λ is the threshold of the band gap absorption). The results are in accordance with monoclinic and tetragonal phases reported in the previous literatures, respectively. It is worth noting that sub-absorption is found in the visible light region (the blue shading in Fig. 6a), which may be attributed to the optical transition of the Nd^{3+} and Er^{3+} impurity levels within the $BiVO_4$ gap [38]. As a result, it can be concluded that the doping can induce new energy levels in the $BiVO_4$ gap.

To further explore the interaction effects of up-conversion property induced by Nd^{3+} and Er^{3+} in co-doped BVO samples, $BiVO_4$ samples absorbance manifesting at 523 nm, 593 nm, 659 nm and 754 nm are plotted v.s. the molar ratio of Nd^{3+} or Er^{3+} (Fig. 6c). As the molar ratio of Nd to Er is increased, the absorbance of doped/co-doped BVO excited by Nd^{3+} is increased at 593 nm and 754 nm while its enhancement rate is decreased at 6:4. By comparison, the

absorbance of the doped/co-doped BVO caused by Er^{3+} is enhanced as the ratio of Er to Nd is arisen, but it is reduced pronouncedly at 4: 6 [39]. Combined with the photocatalytic properties, it can be deduced that Er^{3+} can promote the up-conversion of Nd^{3+}, even by sacrificing its own energy. Therefore, it implies that there should be an energy transfer of up-conversion absorption between Nd^{3+} and Er^{3+} levels, in particular with Nd: Er (molar ratio) = 5:5. On the basis of the analyses at 980 nm in Fig. 6b and c, it can be referred that Nd^{3+} continuously absorbs multiple photons first from the $^4I_{9/2}$ state to $^4F_{5/2} + {}^2H_{9/2}$ states, and then to the $^4K_{15/2} + {}^4G_{9/2}$ states. Finally the photons in the excited states can release a higher energy photon to the $^4I_{9/2}$ ground state so as to finish the energy up conversion process. Similarly, Er^{3+} absorbs multiple photons and jumps from the $^4I_{15/2}$ state to $^4I_{11/2}$ state, and to the $^4F_{9/2}$ state, then jumps back to the $^4I_{15/2}$ ground state and emits the higher energy photons to achieve the up-conversion (Fig. 6d). What's more, it is inferred that there is energy transfer among the $^4H_{11/2}$ and $^4F_{9/2}$ in Er^{3+} ${}^4G_{5/2}$
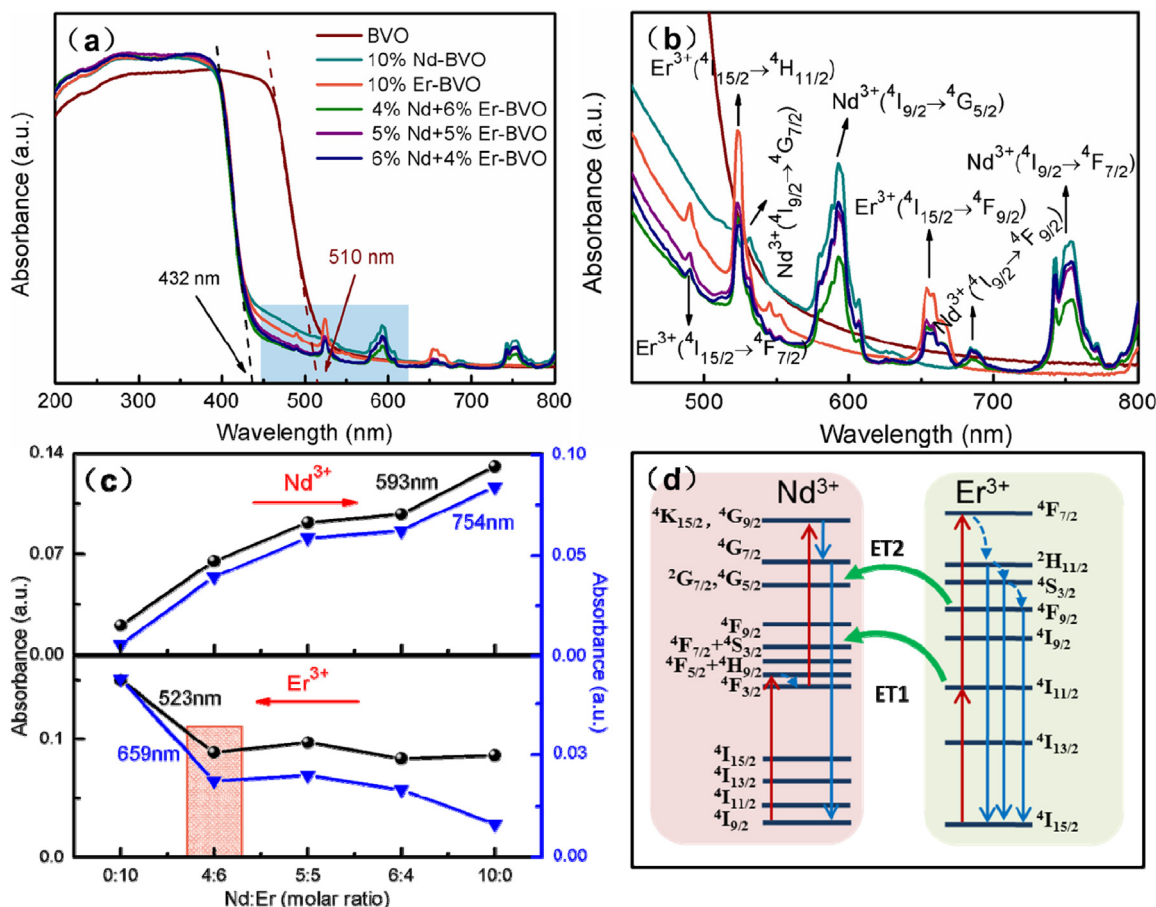
Fig. 6. (a) The UV–vis diffuse reflectance spectra of BiVO₄ samples, (b) The absorbance peaks of the doped BiVO₄ samples at 450–800 nm, (c) Absorption intensity curves of the doped samples at 593 nm, 754 nm, 523 nm and 659 nm, (d) Mechanism of Nd-Er energy transfer in BiVO₄ at 980 nm.

and $^4F_{7/2 \text{ in Nd}}^{3+}$ of co-doped BVO, which can maximize the up-conversion light absorption when Er^{3+} and Nd^{3+} exist at the same time, exhibiting much higher light response than that of single Er^{3+} or Nd^{3+}.

In order to further explore the up conversion mechanism, the photocurrent is discussed to study the near-infrared (NIR) light (750–1500 nm) response of BVO, 10%Nd-BVO, 10%Er-BVO and 5%Nd + 5%Er-BVO samples, as shown in Fig. 7a. It is impossible for BVO to harvest the 750–1500 nm light due to the energy gap (2.4 eV), resulting to no current response. Predictably, the 10%Nd-BVO, 10%Er-BVO and 5%Nd + 5%Er-BVO possess constant photocurrent response during the several intermittent on-off illuminate cycles. Notably, there are two points as follows. Due to the up-conversion property induced by Nd^{3+} and Er^{3+}, the 10%Nd-BVO, 10%Er-BVO and 5%Nd + 5%Er-BVO exhibit distinct photocurrents. Furthermore, if the separation of carriers cannot be promoted by the energy transfer, the observed current of 5%Nd + 5%Er-BVO will be the half of the superposition current of 10%Nd-BVO and 10%Er-BVO as 5%Nd + 5%Er-BVO is composed of half 10%Nd-BVO and half 10%Er-BVO [40]. However, as shown in Fig. 7a, the observed current of 5%Nd + 5%Er-BVO is much higher than the predicted superposition value, indicating the existence of energy transfer between Nd^{3+} and Er^{3+}.

After then, under the same conditions (750–1500 nm), the photodegradation is also characterized over BVO, 10%Nd-BVO, 10%Er-BVO and 5%Nd + 5%Er-BVO (Fig. 7b). It is expected that the photodegradation trend of samples is consistent with the photocurrent of them. The BVO, showing no light response, has almost no degradation under the NIR irradiation. However, the 10%Nd-

BVO and 10%Er-BVO has significant degradation, especially that of 5%Nd + 5%Er-BVO can be up to the 90% within 20 min. The outstanding degradation of 5%Nd + 5%Er-BVO is attributed to the up-conversion and the energy transfer.

In the previous analysis, RhB molecules are absorbed when the light wavelength is 535 nm while the BVO and 5%Nd + 5%Er-BVO poorly respond to it. Further, the activities of BVO and 5%Nd + 5%Er-BVO have shown with the light wavelength at 535 nm (Fig. S2). The degradation rate of BVO has only 10% or so after 150 min of irradiation, indicating that the photosensitized mechanism exists in BiVO₄. According to the 5%Nd + 5%Er-BVO, 60% of degradation rate is mainly attributed to the up-conversion property while is light conversion from 535 nm to shorter than 535 nm, and also due to the sensitized mechanism. Owing to the main active species (holes) and small photosensitized degradation rate, photosensitized mechanism is not the primary role in the photocatalytic degradation under simulated sunlight even if it does exist.

Furthermore, the doping behavior has a great influence on the native energy band structure of BiVO₄, and the flat band potentials (E_{FB}) are calculated from the Mott-Schottky plots to analyze the E_{CB} and E_{VB} values of BiVO₄ (Fig. 8a). After data fitting and converting, the estimated horizontal intercepts of the linear segments are −0.19 V, −0.13 V, −0.15 V and −0.11 V vs. Ag/AgCl (0.2355 V) and then calculated into −0.25 V, −0.19 V, −0.21 V and −0.17 V vs. NHE, which are approximately used as E_{CB} values. The details values of E_{CB} and E_{VB} of the above samples are shown in the inset of Fig. 8a. The doping leads to distortion of crystal lattice of BiVO₄ in XRD analyses which causes the positive shifts of E_{VB} to different degrees in BiVO₄, endowing the higher oxidation potential to h^+. As h^+ is the
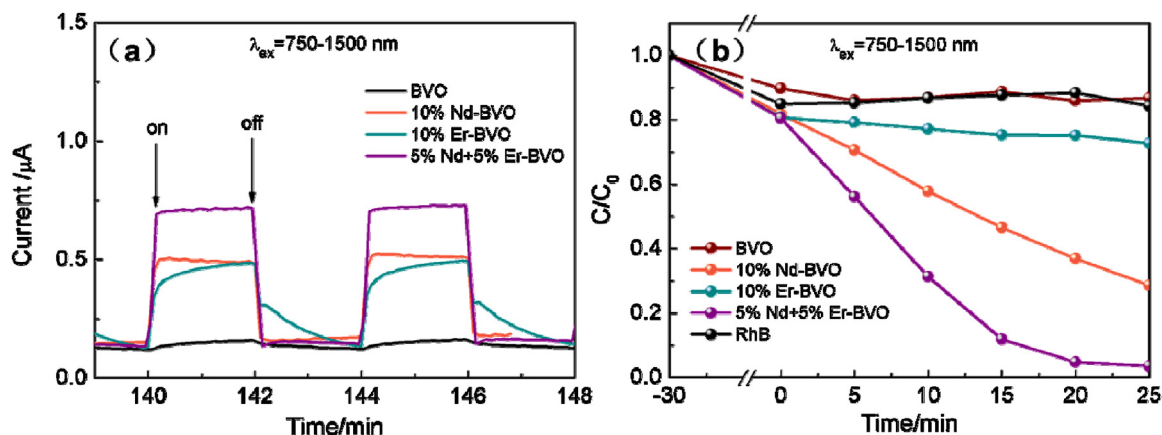
Fig. 7. (a) Amperometric i–t curves and (b) degradation process of RhB for BVO, 10%Nd-BVO, 10%Er-BVO and 5%Nd + 5%Er-BVO samples under the wavelength region of 750–1500 nm.
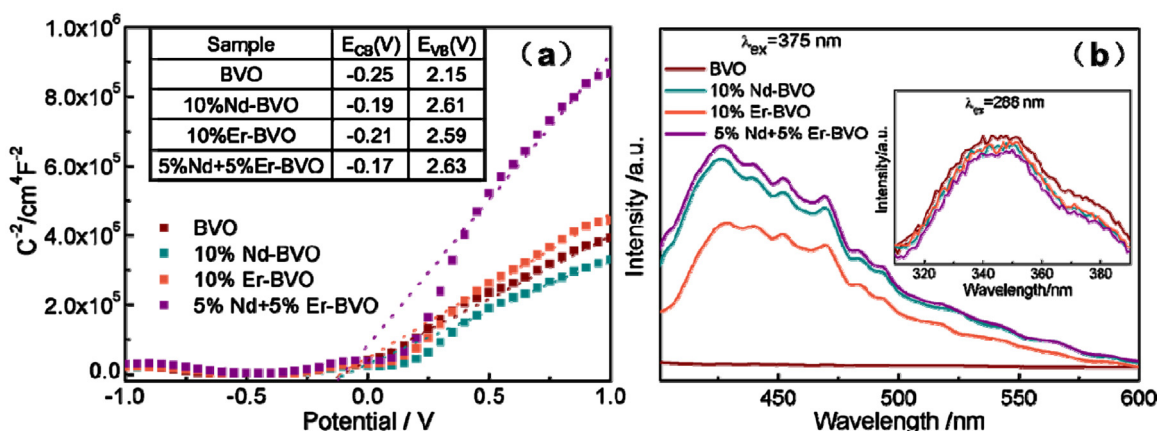

Fig. 8. (a) Mott-schottky plots and (b) PL spectra of BVO, doped BVO and 5%Nd + 5%Er-BVO.

main active species (Fig. 5a), the more positive the E_{VB} shifts, the higher degradation rate will be, which is in good accordance with the degradation curves. Therefore, the more positive E_{VB} of $BiVO_4$ is the vital factor to improve its degradation performance.

PL spectral measurement is carried out to reveal the migration, transfer, and recombination processes of photogenerated electron-hole pairs in the semiconductor materials [41]. In most cases, the decreased recombination ratio of the electron-hole pairs can facilitate the photocatalytic reaction. According to the previous results of PL spectra (Fig. 8b), the samples except for the pure BVO show obvious fluorescent peaks induced by the fluorescent effect of Nd^{3+} and Er^{3+} (Nd^{3+} and Er^{3+} can emit photons to present the fluorescence phenomenon under optical excitation), which cannot directly reflect the recombination rate. In order to further figure it out, we use other incident light wavelength ($\lambda = 288$ nm) to obtain the emission spectra (inset of Fig. 8b), which can eliminate the fluorescent disturbance induced by Nd^{3+} and Er^{3+}. The same shape fluorescence emission of them at the range of 310–390 nm means that the peak belongs to $BiVO_4$. Predictably, the PL emission intensity of 10%Nd-BVO, 10%Er-BVO and 5%Nd + 5%Er-BVO is weaker than that of BVO, especially the 5%Nd + 5%Er-BVO. The lower recombination rate of carriers in 10%Nd-BVO, 10%Er-BVO and 5%Nd + 5%Er-BVO, indicating that the doping behavior can induce much higher separation rate of carriers. The higher separation rate can be ascribed to the impurity energy level in the gap of the 10%Nd-BVO, 10%Er-BVO and 5%Nd + 5%Er-BVO, suggested by the lattice distortion induced by substitution and extra absorption region induced by surface defects in XRD and UV–vis DRS results.

Such impurity energy level can capture photoexcited electrons to suppress the recombination of carriers. The new energy levels can influence the photocarriers' generation-separation-transfer efficiency in two aspects. On one hand, defects and surface traps in the levels act as the capture centers to trap photogenerated electrons [27], resulting in the increased separation rate and apply the more active holes to participate in the oxidation reactions. On the other hand, the impurity energy level brings important up-conversion effect. Such up-conversion can convert the lower energy light into the higher energy light. Additionally, surprising synergetic energy transfer occurs between Nd^{3+} and Er^{3+} which can maximize the up-conversion effect, resulting in the overall higher light absorption of co-doped BVO. Consequently, the separation efficiencies of co-doped BVO are much higher on the basis of greatly enhanced light absorptions, leaving much more active photocarriers for the following photocatalytic performance, among which the 5%Nd + 5%Er-BVO sample shows the highest photocatalytic degradation rate of over 96% after the simulated sunlight irradiation for 150 min and NIR irradiation for 20 min.

Based on the above analyses, it can be concluded that the Nd^{3+} and Er^{3+} play a significant role on the photocatalytic performance of the co-doped BVO samples. To understand the roles of Nd^{3+} and Er^{3+}, the mechanism of the co-doped BVO photocatalytic reaction is proposed in Fig. 9 [32,33]. Firstly, Nd^{3+} and Er^{3+} dopants result in the lattice distortions since they enter into the $BiVO_4$ and substitute Bi^{3+} sites, forming impurity energy levels in $BiVO_4$. The new energy level can trap the electrons, improving the carrier separation efficiency and leaving more active holes to participate in the oxidation
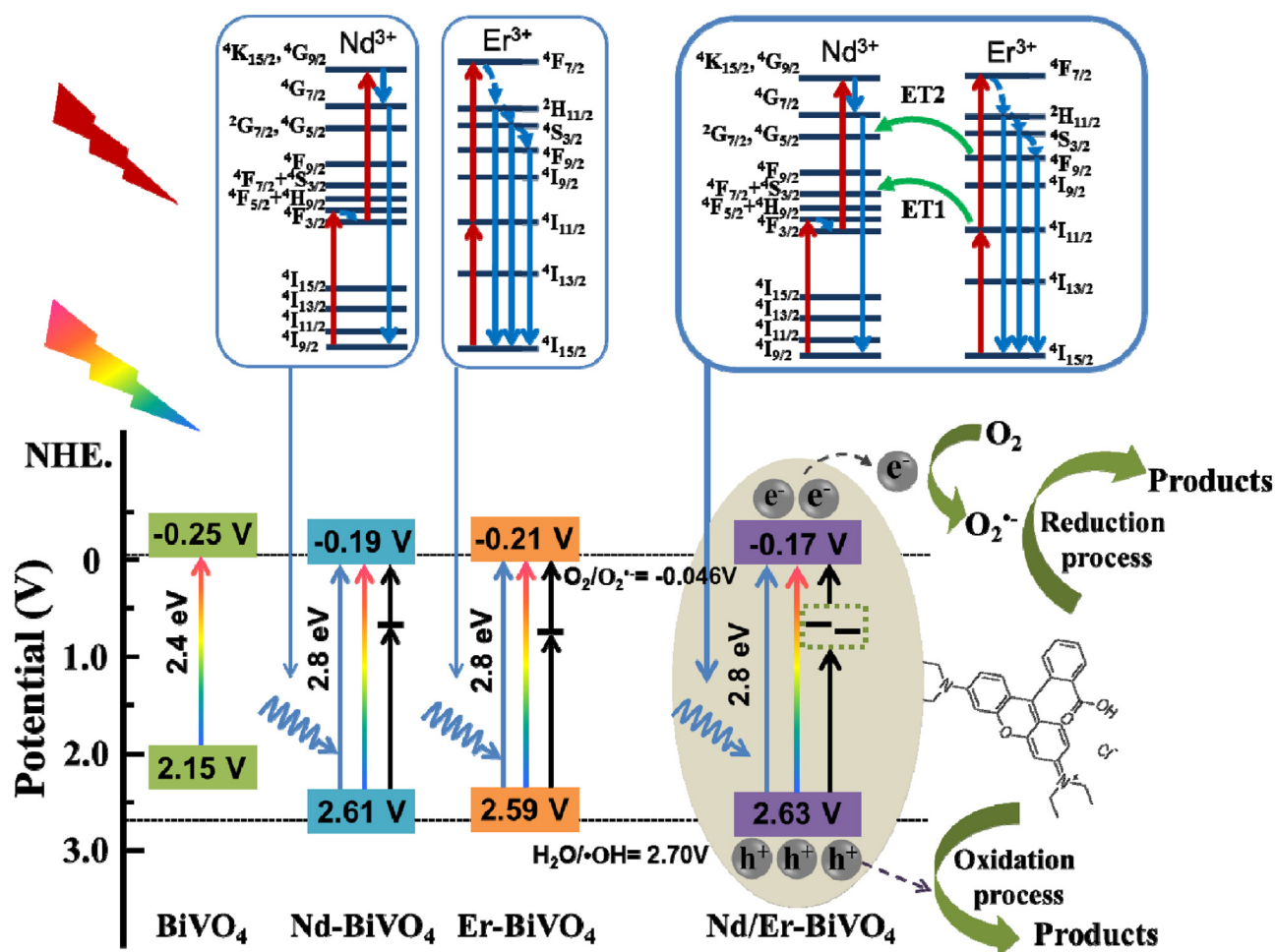
Fig. 9. The schematic diagram of the proposed mechanism for photocatalytic reactions of BiVO₄ before and after doping Nd/Er.

reactions. Apart from the trapping effect, synergetic energy transfer occurs between the up-conversion light absorptions of Nd^{3+} and Er^{3+}, which can maximize the up-conversion effect. Therefore, the actual separation efficiencies of co-doped BVO are much higher on the basis of greatly enhanced light absorptions, leaving much more active photocarriers. Second, co-doped BVO obtain a tetragonal phase with lattice distortions and lead to more optimized energy band structures. As the main active species in degradation, h^+ in the valence band with more positive potentials are more favorable for the degradation of organic pollutants into inorganic small molecules. Due to the synergistic effect of the above mechanisms, 5%Nd + 5%Er-BVO obtains the most excellent photocatalytic performance, making it a potential candidate material for application of organic pollutant degradation.

4. Conclusions

The tetragonal Nd/Er co-doped BiVO₄ photocatalysts have been obtained by microwave hydrothermal method. The substitution of Nd^{3+} and Er^{3+} for the Bi^{3+} sites in BiVO₄ leads to the $[VO_4]$ tetragonal chains distortion and induces phase translation from the monoclinic- into tetragonal-structure, resulting in the external morphologies evolution from particle aggregates into rod-particle aggregates. The co-doping with the most significant lattice distortion can induce impurity energy levels in BiVO₄ to trap the electrons, improving the carrier separation efficiency and leaving more active holes to participate in the oxidation reactions. Moreover, the energy transfer occurs among the $^4H_{11/2}$ and

$^4F_{9/2\,in\,Er}{}^{3+4}G_{5/2}$ and $^4F_{7/2\,in\,Nd}{}^{3+}$ of co-doped BiVO₄, which can exhibit much higher up-conversion light response. The co-doped BiVO₄ obtains a tetragonal phase with lattice distortions and leads to more positive VB potentials. As the main active species in degradation, h^+ in the valence band with more positive potentials are more favorable for the degradation of organic pollutants into inorganic small molecules. Finally, the degradation rate can reach the highest 96% in 150 min under simulated sunlight light and 20 min under NIR irradiation, giving rise to the co-doping of Er^{3+} and Nd^{3+} an efficient way to modify BiVO₄ for its active application.

Appendix A. Supplementary data

Supplementary data associated with this article can be found, in the online version, at http://dx.doi.org/10.1016/j.apcatb.2017.05.018.

References

[1] X. Zhang, G. Zuo, X. Lu, C. Tang, S. Cao, M. Yu, J. Colloid Interface Sci. 490 (2017) 774–782.
[2] X.F. Zhang, Y.N. Wang, B.S. Liu, Y.H. Sang, H. Liu, Appl. Catal. B—Environ. 202 (2017) 620–641.
[3] J.X. Sun, G. Chen, J.Z. Wu, Appl. Catal. B—Environ. 179 (2015) 54–60.
[4] O. Monfort, S. Sfaelou, L. Satrapinskyy, T. Plecenik, T. Roch, G. Plesch, P. Lianos, Catal. Today 280 (2017) 51–57.
[5] L. Zhou, W. Wang, S. Liu, L. Zhang, H. Xu, W. Zhu, J. Mol. Catal. A: Chem. 252 (2006) 120–124.
[6] Y. Park, K.J. McDonald, K.S. Choi, Chem. Soc. Rev. 42 (2013) 2321–2337.
[7] G.Q. Tan, L.L. Zhang, H.J. Ren, S.S. Wei, J. Huang, A. Xia, ACS Appl. Mater. Interfaces 5 (2013) 5186–5193.
[8] H. Xu, C.D. Wu, H.M. Li, J.Y. Chu, G.S. Sun, Y.G. Xu, Y.S. Yan, Appl. Surf. Sci. 256 (2009) 597–602.
[9] Y. Wang, F.Y. Liu, Y.J. Hua, C.T. Wang, X.D. Zhao, X.Y. Liu, H.D. Li, J. Colloid Interface Sci. 483 (2016) 307–313.
[10] Y. Luo, G. Tan, G. Dong, H. Ren, A. Xia, Appl. Surf. Sci. 364 (2016) 156–165.
[11] C. Regmi, Y.K. Kshetri, S.K. Ray, R.P. Pandey, S.W. Lee, Appl. Surf. Sci. 392 (2017) 61–70.
[12] J. Wang, X.Y. Chong, R. Zhou, J. Feng, Scr. Mater. 126 (2017) 24–28.
[13] Y. Zhang, Z. Yi, G. Wu, Q. Shen, J. Photochem. Photobiol. A 327 (2016) 25–32.
[14] C. Adan, J. Marugan, S. Obregon, G. Colon, Appl. Catal. A—Gen. 526 (2016) 126–131.
[15] S. Xue, H. He, Z. Wu, C. Yu, Q. Fan, G. Peng, K. Yang, J. Alloy Compd. 694 (2017) 989–997.
[16] D. Zhou, L.X. Pang, J. Guo, Z.M. Qi, T. Shao, Q.P. Wang, H.D. Xie, X. Yao, C.A. Randall, Inorg. Chem. 53 (2014) 1048–1055.
[17] S. Usai, S. Obregon, A.I. Becerro, G. Colon, J. Phys. Chem. C 117 (2013) 24479–24484.
[18] Y. Luo, G. Tan, G. Dong, L. Zhang, J. Huang, W. Yang, C. Zhao, H. Ren, Appl. Surf. Sci. 324 (2015) 505–511.
[19] W. Yang, G.Q. Tan, H.J. Ren, L.L. Zhang, C.C. Zhao, A. Xia, RSC Adv. 5 (2015) 7324–7329.
[20] Y. Luo, G. Tan, G. Dong, H. Ren, A. Xia, Ceram. Int. 41 (2015) 3259–3268.
[21] S. Obregón, G. Colón, Appl. Catal. A—Gen. 501 (2015) 56–62.
[22] L.W. Shan, Y.T. Liu, J. Mol. Catal. A—Chem. 416 (2016) 1–9.
[23] S. Obregón, G. Colón, Appl. Catal. B—Environ. 152–153 (2014) 328–334.
[24] M. Shang, W.Z. Wang, L. Zhou, S.M. Sun, W.Z. Yin, J. Hazard. Mater. 172 (2009) 338–344.
[25] A. Zhang, J. Zhang, J. Hazard. Mater. 173 (2010) 265–272.
[26] O.F. Lopes, K.T.G. Carvalho, A.E. Nogueira, W. Avansi, C. Ribeiro, Appl. Catal. B—Environ. 188 (2016) 87–97.
[27] N. Tian, Y. Zhang, H. Huang, Y. He, Y. Guo, J. Phys. Chem. C 118 (2014) 15640–15648.
[28] M. Wang, Y.S. Che, C. Niu, M.Y. Dang, D. Dong, J. Hazard. Mater. 262 (2013) 447–455.
[29] X. Gao, Z. Wang, X. Zhai, F. Fu, W.H. Li, J. Mol. Liq. 211 (2015) 25–30.
[30] C. Karunakaran, S. Kalaivani, P. Vinayagamoorthy, S. Dash, Mater. Sci. Eng. B—Adv. 187 (2014) 53–60.
[31] K.F. Zhang, Y.X. Liu, J.G. Deng, S.H. Xie, H.X. Lin, X.T. Zhao, J. Yang, Z. Han, H.X. Dai, Appl. Catal. B—Environ. 202 (2017) 569–579.
[32] Y.X. Liu, H.X. Dai, J.G. Deng, L. Zhang, C.T. Au, Nanoscale 4 (2012) 2317–2325.
[33] G.Q. Li, Y. Bai, W.F. Zhang, Mater. Chem. Phys. 136 (2012) 930–934.
[34] S. Obregón, G. Colón, Appl. Catal. B—Environ. 158–159 (2014) 242–249.
[35] C.S. Lim, V.V. Atuchin, A.S. Aleksandrovsky, M.S. Molokeev, A.S. Oreshonkov, J. Alloy Compd. 695 (2017) 737–746.
[36] J.X. Sun, G. Chen, J.Z. Wu, Appl. Catal. B—Environ. 179 (2015) 54–60.
[37] M. Xu, W.D. Zhang, J. Solid State Chem. 227 (2015) 247–254.
[38] C.H. Lu, P. Zhang, S.J. Jiang, X. Wu, S.Q. Song, M.S. Zhu, Z.Z. Lou, Z. Li, F. Liu, Y.H. Liu, Y. Wang, Z.G. Le, Appl. Catal. B—Environ. 200 (2017) 378–385.
[39] Y.J. Shao, Q.H. Yang, Y. Gui, Y. Yuan, Q. Lu, J. Alloy Compd. 667 (2016) 76–81.
[40] J.H. Wang, H. Li, S.G. Meng, Appl. Catal. B—Environ. 200 (2017) 19–30.
[41] L. Ge, C. Han, J. Liu, Appl. Catal. B—Environ. 108–109 (2011) 100–107.